Electronic Supplementary Material (ESI) for Chemical Science.

Supporting Information

Electron Delocalization of Robust High-nuclear Bismuth-oxo Clusters for Promoted CO_2 Electroreduction

Baoshan Hou[+], Haiyan Zheng[+], Kunhao Zhang, Qi Wu, Chao Qin, Chunyi Sun*, Qinhe Pan, Zhenhui Kang, Xinlong Wang* and Zhongmin Su

Dr. B. Hou, H. Zheng, Q. Wu, Prof. C. Qin, C. Sun, X. Wang,

Key Lab of Polyoxometalate Science of Ministry of Education, National & Local United Engineering Laboratory for Power Battery Institution. Northeast Normal University. Changchun, Jilin, 130024 (China)

E-mail: suncy009@nenu.edu.cn, wangxl824@nenu.edu.cn

Prof. Q. Pan, X. Wang, Z. Su

Key Laboratory of Advanced Materials of Tropical Island Resources, Ministry of Education, Hainan University, Haikou, 570228 (China)

Dr. K. Zhang

Shang hai Synchrotron Radiation Facility (SSRF), 239 Zhangheng Road, Pudong New District, Shanghai, 200120 (China)

Prof. Z. Kang

Institute of Functional Nano & Soft Materials (FUNSOM), Jiangsu Key Laboratory for Carbon-Based Functional Materials & Devices, Soochow University, Suzhou 215123 Jiangsu, China.

Experimental Procedures

General Experimental Section

All the reagents were obtained from commercial sources and used without further purification. Powder X-ray diffraction (PXRD) patterns were recorded ranging from 5 to 50º at room temperature on a Siemens D5005 diffractometer with Cu Kα (λ = 1.5418 Å). The C, H and N elemental analyses were conducted on a Perkin–Elmer 2400CHN elemental analyzer. Thermogravimetric analysis (TGA) of the samples were performed using a Perkin–Elmer TG–7 analyzer heated from room temperature to 800 ºC under nitrogen at the heating rate of 10 °C·min^{-1}. IR spectrum was performed in the range 4000–400 cm^{-1} using KBr pellets on an Alpha Centaurt FT/IR spectrophotometer. X-ray photoelectron spectroscopy (XPS) characterizations were performed on an Escalab 250 instrument. Scanning electron microscopy (SEM, Hitachi, SU–70) was utilized to obtain the morphology and structure of the samples. In situ IR was carried out on a 6700 Flex FTIR spectrometer equipped with a smart iTRTM attenuated total reflectance (ATR) sampling accessory in the range of 500–4000 cm^{-1}. In situ Raman measurements were carried out by using a 785 nm diode laser with the power of 10 mW and a Raman spectrometer (iHR 550, Symphony II, Horiba Jobin Yvon).

Synthesis of BiOC–1

A mixture of TBC[8] (50 mg), $Bi(NO_3)_3$ (50 mg) was dissolved in CH_3OH (10 mL) and en (0.2 mL). The mixture was transferred into a Parr Teflon–lined autoclave and kept at 130 °C for 72 h. After cooling down to room temperature, the pale yellow bulk crystals were obtained and washed with CH_3OH (yield: 82 % based on Bi). Elemental analysis (%): calculated for **BiOC–1**, C 47.70, H 5.73, N 1.14; found, C 47.82, H 5.85, N 1.29.

Synthesis of BiOC–2

A mixture of TBC[8] (50 mg), $Bi(NO_3)_3$ (50 mg) was dissolved in CH_3OH (10 mL) and en (0.2 mL). The mixture was transferred into a Parr Teflon–lined autoclave and kept at 100 °C for 72 h. After cooling down to room temperature, the pale yellow bulk crystals were obtained and washed with CH_3OH (yield: 12 % based on Bi).

Synthesis of BiOC–3

A mixture of TBC[8] (40 mg), $Bi(NO_3)_3$ (30 mg), $Al(NO_3)_3$ (10 mg) was dissolved in DMF (5 mL), CH_3OH (5 mL) and en (0.2 mL). The mixture was transferred into a Parr Teflon–lined autoclave and kept at 130 °C for 72 h. After cooling down to room temperature, the yellow flake crystals were obtained and washed with CH_3OH (yield: 78 % based on Bi). Elemental analysis (%): calculated for **BiOC–3**, C 48.03, H 5.05, N 0.31; found, C 48.22, H 5.15, N 0.45.

Synthesis of BiOC–4

A mixture of TBC[8] (30 mg), $Bi(NO_3)_3$ (30 mg) was dissolved in DMF (5 mL), CH_3OH (5 mL) and en (0.2 mL). The mixture was transferred into a Parr Teflon–lined autoclave and kept at 130 °C for 72 h. After cooling down to room temperature, the light yellow massive crystals were obtained and washed with CH_3OH (yield: 71 % based on Bi). Elemental analysis (%): calculated for **BiOC–4**, C 38.33, H 4.25, N 1.36; found, C 38.22, H 4.15, N 1.45.

Synthesis of BiOC–5

A mixture of TBC[8] (50 mg), $Bi(NO_3)_3$ (50 mg) was dissolved in DMF (2 mL), CH_3OH (5 mL) and en (0.2 mL). The mixture was transferred into a Parr Teflon–lined autoclave and kept at 130 °C for 72 h. After cooling down to room temperature, the yellow octahedral or poke–shaped crystals were obtained and washed with CH_3OH (yield: 73 % based on Bi). Elemental analysis (%): calculated for **BiOC–5**, C 40.11, H 4.47, N 0.73; found, C 40.22, H 4.65, N 0.94.

Synthesis of BiOC–6

A mixture of TBC[8] (50 mg), $Bi(NO_3)_3$ (30 mg), Molybdic acid (10 mg) was dissolved in DMF (2 mL), CH_3OH (8 mL) and en (0.2 mL). The mixture was transferred into a Parr Teflon–lined autoclave and kept at 130 °C for 72 h. After cooling down to room temperature, the light yellow small grain crystals were obtained and washed with CH_3OH (yield: 5 % based on Bi). Elemental analysis (%): calculated for **BiOC–6**, C 53.09, H 6.93, N 5.71; found, C 52.22, H 6.55, N 5.84.

The preparation of the working electrode

10 mg of samples were added to a 1 mL solution containing ethanol (100μL) water (800μL) and Nafion solution (5wt%, 100 μL) to produce a suspension. After sonicating for 30 min, 25 μL uniformly mixed suspension was dropped onto a hydrophobic carbon paper (1 × 2 cm) to form a 1×1 cm^2 catalyst area with a catalyst loading density of ~0.5 mg cm^{-2}.

Electrochemical measurements

All electrochemical tests of the catalysts were performed on a CHI–760E electrochemical workstation at room temperature and under ambient conditions. An airtight H–type cell separated by a cation exchange membrane (Nafion®117, dupont) was used as a reactor. Each compartment contained 30 mL electrolyte with approximately 20 mL headspace. Ag/AgCl electrode (saturated KCl) and carbon rod were used as the reference electrode and the counter electrode, respectively. The working electrode was a catalyst–modified carbon paper (1 cm × 2 cm). The polarization curves results were obtained by performing linear sweep voltammetry (LSV) mode with a scan rate of 5 mV s^{-1}. Potentials were measured against an Ag/AgCl reference electrode and the results were converted to those against a reversible hydrogen electrode (RHE) based on the RHE calibration. All the curves were presented without IR compensation.

The product analysis

The gaseous reduction products of CO_2 reduction reaction were monitored by Shimadzu Gas Chromatography (GC). The electrolyte solution was collected from the cathode chamber after electrolysis to analyze liquid products and characterized by 1H–NMR and ion chromatography. The ion chromatograph was equipped with a Shodex IC SI–52 4E anion separation column with an eluent of 0.07 mmol L^{-1} Na_2CO_3.

The $FE_{products}$ was calculated according to the following equation:

$$FE_{products} = \frac{N \times F \times n_{products}}{Q} \times 100\%$$

Where N is the number of electrons transferred for products. (N = 2 for CO_2 to HCOOH and CO conversion and H_2O to H_2 conversion), F is the Faraday constant (96485 C/mol), $n_{products}$ is the moles of produced products (mol), and Q is the total charge obtained from chronoamperometry (C).

The TOF for HCOOH was calculated as follow:

$$TOF = \frac{I_{product} NF}{m_{cat} \times \omega / M_{Bi}} \times 3600$$

$I_{product}$: partial current for certain product, HCOOH;
N: the number of electron transferred for product formation, which is 2 for HCOOH;
F: Faradaic constant, 96485 C mol^{-1};
m_{cat}: catalyst mass in the electrode, g;
ω: Bi loading in the catalyst;
M_{Bi}: atomic mass of Bi, 208.98 g mol^{-1}.

Computational details

All the calculations are performed within the framework of DFT implemented in the Vienna ab initio simulation package (VASP).[1–3] The generalized gradient approximation with the function is described by the Perdew–Burke–Ernzerhof type (PBE).[4] The projector–augmented wave (PAW) method[5] is applied to describe the wavefunctions in the core regions, while the valence wavefunctions are expanded as linear combination of plane–waves with a cutoff energy of 400 eV. The total energy is converged to 10^{-5} eV in the geometry optimizations, and the Hellmann–Feynman force on each relaxed atom is less than 0.02 eV/Å.[6–7]
Gibbs reaction free energy of reaction for CO_2RR elementary steps involving (H^+ + e^-) pair transfer was calculated using computational hydrogen electrode (CHE) model.[8] At U=0 V, $\Delta G = \Delta E + \Delta E_{ZPE} - T\Delta S + C_P dT$, where ΔE is the reaction energy difference between the product and reactant of the CO_2RR occurring on catalysts, which can be directly obtained from DFT computations; ΔE_{ZPE}, $T\Delta S$ and $C_p dT$ are zero–point energy correction, entropy correction and enthalpic temperature correction at T=298.15 K respectively, which were calculated from the vibrational frequencies.
The vertical ionization energy for BiOC-4 versus BiOC-5 in the Gaussian16 package,[9] and to conserve computational resources, we simplified the tert butyl groups of the end groups of the crystal materials, we used the B3LYP functional during the calculations,[10,11] 6-311G basis sets for C, H, and O atoms, and Lanl2dz basis sets for Bi. The ODI values of LUMO orbitals of materials using Gaussian 16 software combined with multiwfn3.8 software.[12,13]

Crystal data collection and refinements

All data collections were performed on a Bruker D8–Venture diffractometer with a TurboX–ray Source (Cu Kα radiation, λ = 1.5418 Å) adopting the direct drive rotating anode technique and a CMOS detector at 173 K. The data frames were collected

using the program APEX 3 and processed using the program SAINT routine in APEX 3. The structures were solved by direct methods and refined by the full matrix least–squares on F^2 using the SHELXL–2014 program. The diffused electron densities resulting from these residual solvent molecules were removed from the data set using the SQUEEZE routine of PLATON and refined further using the data generated. The restrained DFIX, SIMU, ISOR instructions were used to make the structures more reasonable. The formula unit was obtained through a combination of elemental analyses and thermogravimetric characterization. CCDC numbers of 2236082 for **BiOC–1**, 2236083 for **BiOC–2**, 2236084 for **BiOC–3**, 2236085 for **BiOC–4**, 2236086 for **BiOC–5**, 2236087 for **BiOC–6**.

Results and Discussion

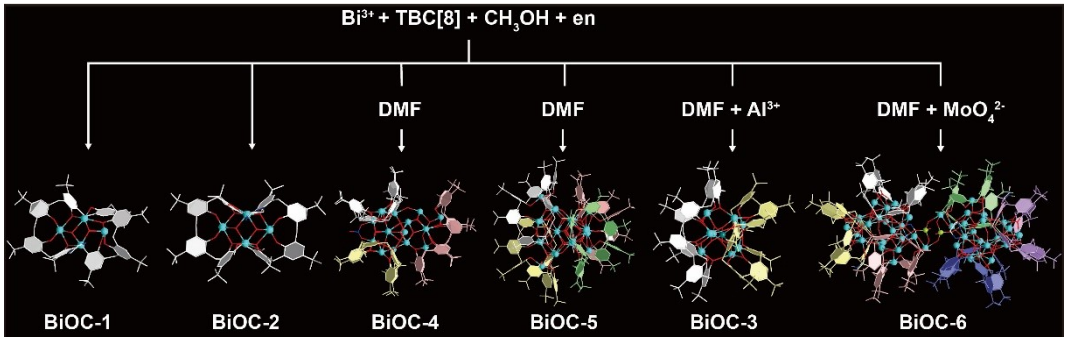

Figure S1. Synthesis of the BiOCs.

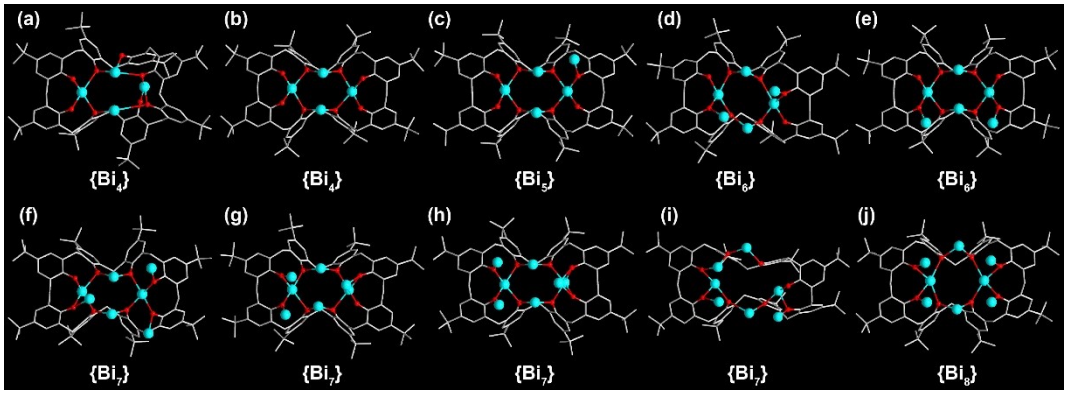

Figure S2. Bi_4–Bi_8 subunits in BiOCs. (a) Bi_4 subunit in **BiOC–1**. (b) Bi_4 subunit in **BiOC–2**. (c) Bi_5, (e) Bi_6 and (f) Bi_7 subunits in **BiOC–4**. (d) Bi_6 subunit in **BiOC–3**. (g) Bi_7 subunit in **BiOC–5**. (h) Bi_7, (i) Bi_7 and (j) Bi_8 subunits in **BiOC–6**.

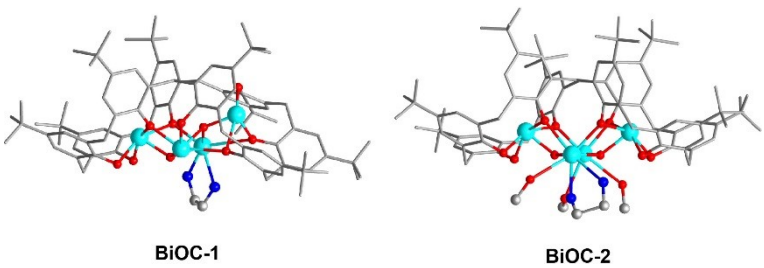

Figure S3. A comparison of the crystal structures of **BiOC–1** and **BiOC–2**.

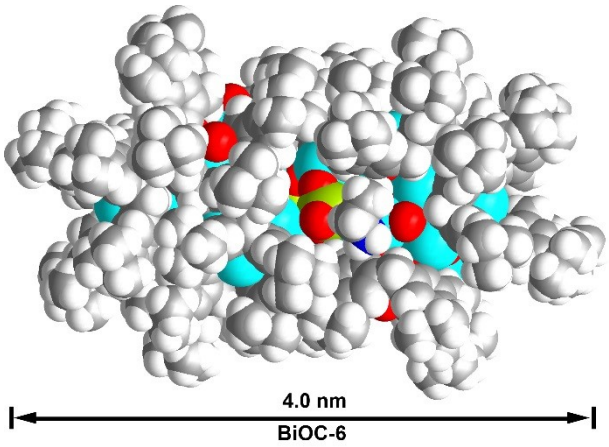

Figure S4. The structures of **BiOC–6**.

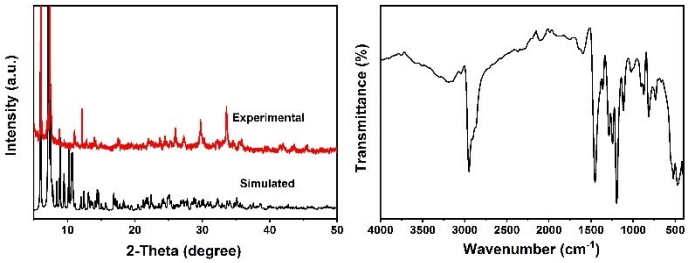

Figure S5. PXRD pattern and FT–IR spectrum for **BiOC–1.**

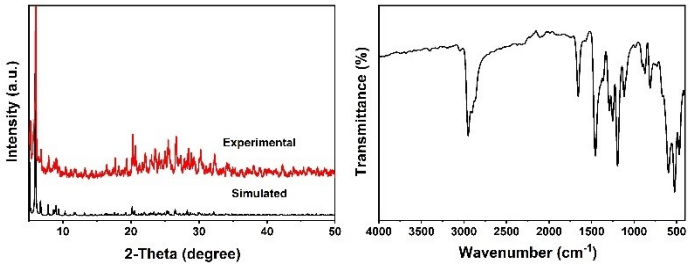

Figure S6. PXRD pattern and FT–IR spectrum for **BiOC–3**.

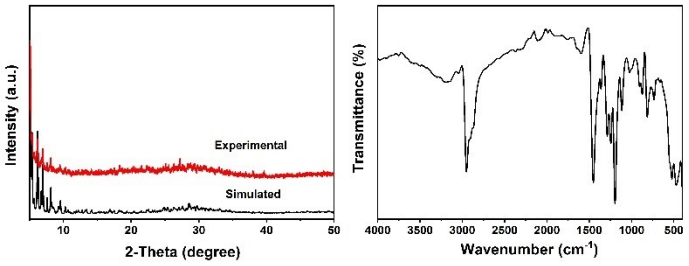

Figure S7. PXRD pattern and FT–IR spectrum for **BiOC–4**.

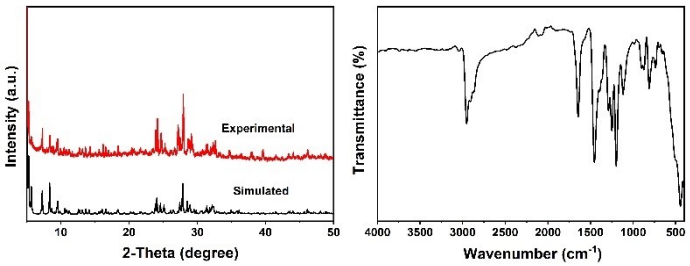

Figure S8. PXRD pattern and FT–IR spectrum for **BiOC–5**.

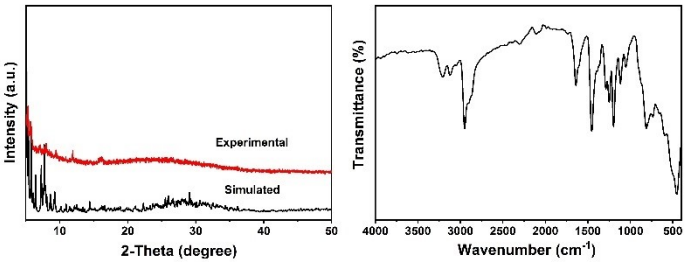

Figure S9. PXRD pattern and FT–IR spectrum for **BiOC–6**.

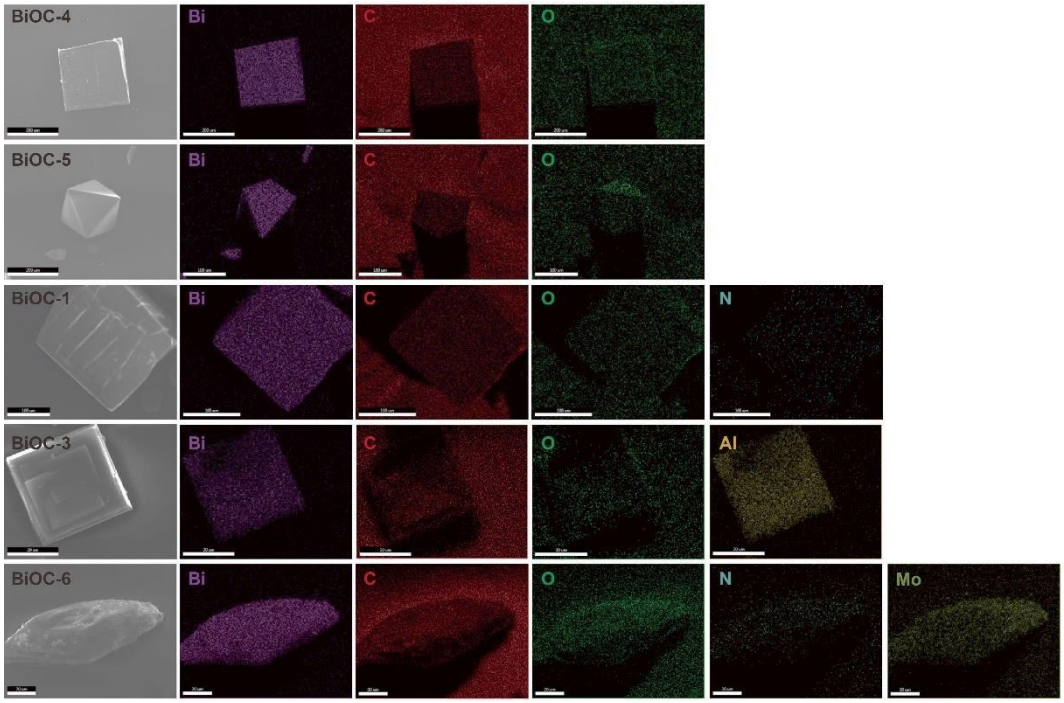

Figure S10. The SEM images and elemental mapping of **BiOC–4**, **BiOC–5**, **BiOC–1**, **BiOC–3** and **BiOC–6**.

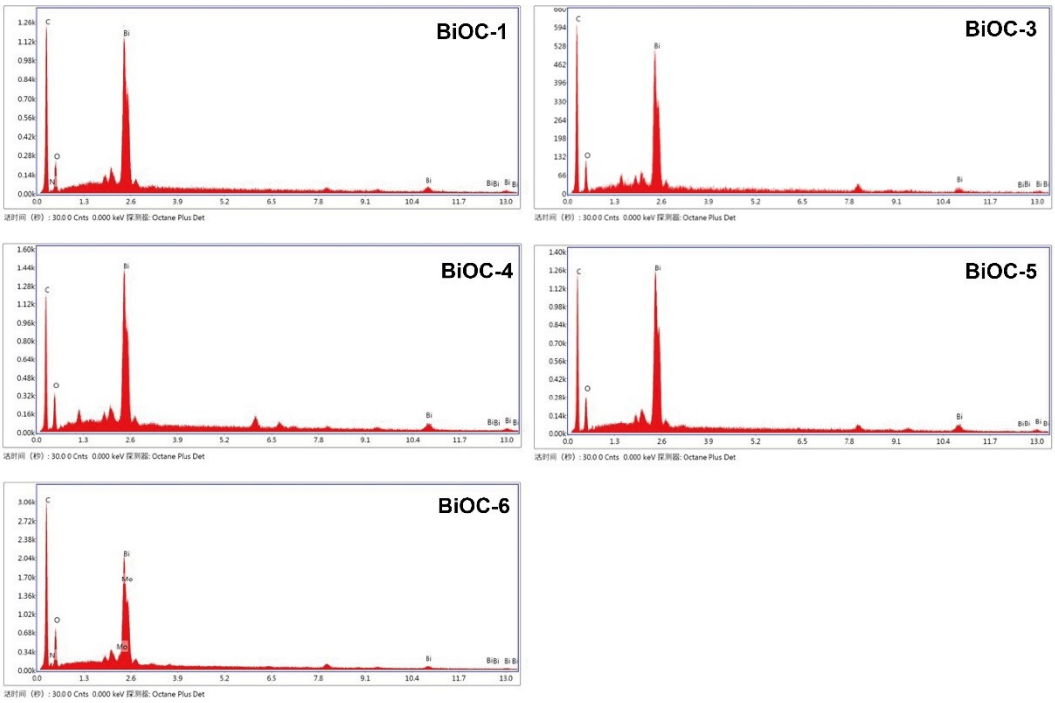

Figure S11. The EDS spectra of **BiOC–1**, **BiOC–3**, **BiOC–4**, **BiOC–5** and **BiOC–6**.

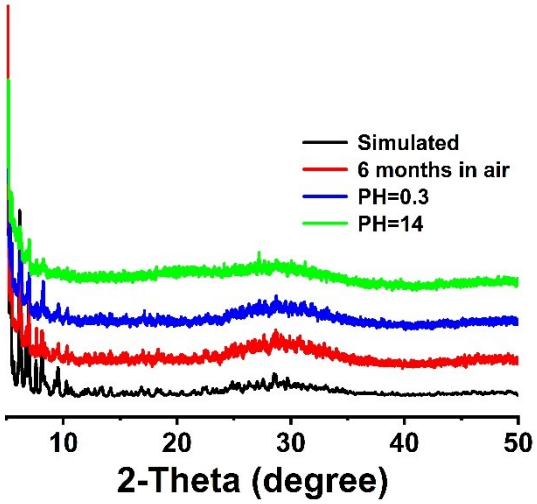

Figure S12. The PXRD patterns of **BiOC–4** treated in air and different pH solutions.

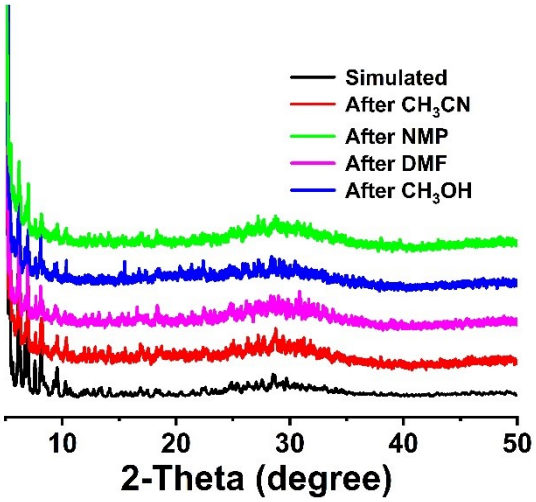

Figure S13. PXRD patterns of **BiOC–4** after being treated in different organic solvents for 24 h.

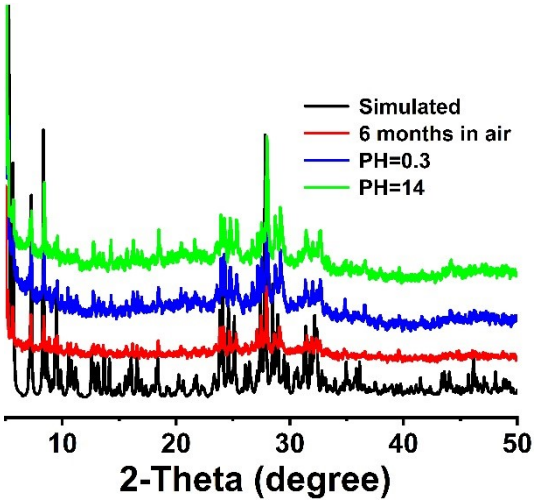

Figure S14. The PXRD patterns of **BiOC–5** treated in air and different pH solutions.

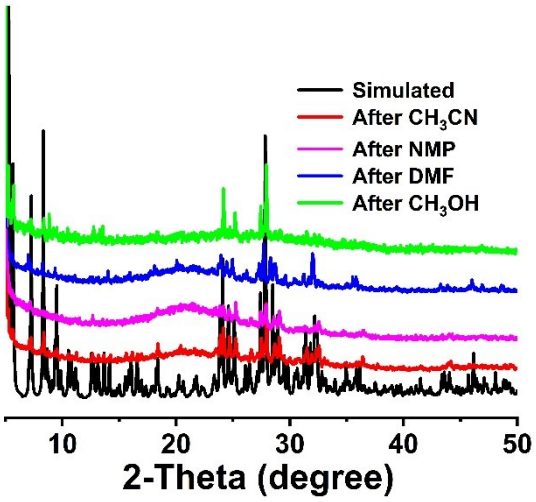

Figure S15. PXRD patterns of **BiOC–5** after being treated in different organic solvents for 24 h.

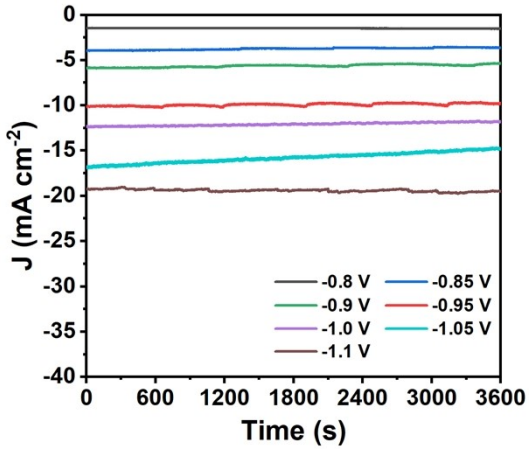

Figure S16. Chrono–amperometric I–t plot at different potentials (V vs. RHE) for **BiOC–4**.

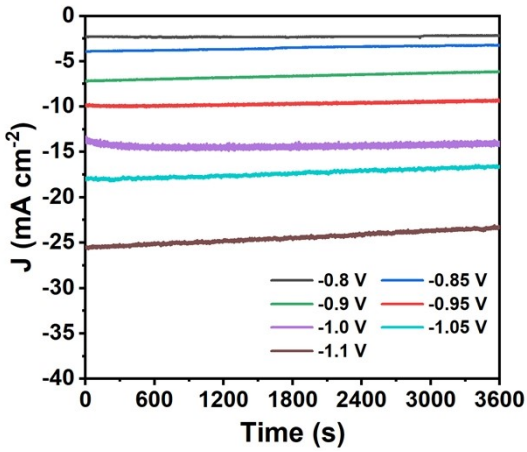

Figure S17. Chrono–amperometric I–t plot at different potentials (V vs. RHE) for **BiOC–5**.

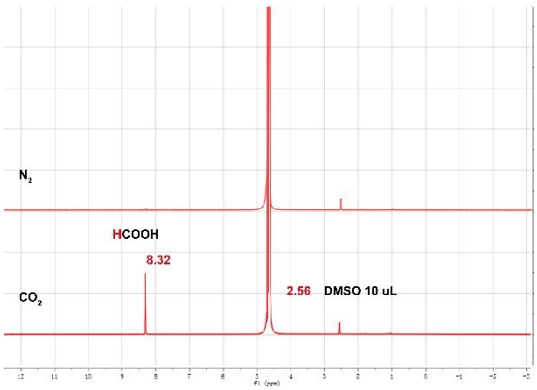

Figure S18. Representative 1H NMR spectra obtained from the catholyte (30 mL) of CO_2 reduction **BiOC–5** at –0.95 V vs. RHE in 0.5 M $KHCO_3$. DMSO is used as an internal standard for quantification of liquid products (10 uL DMSO, 200 uL D_2O and 500 uL catholyte).

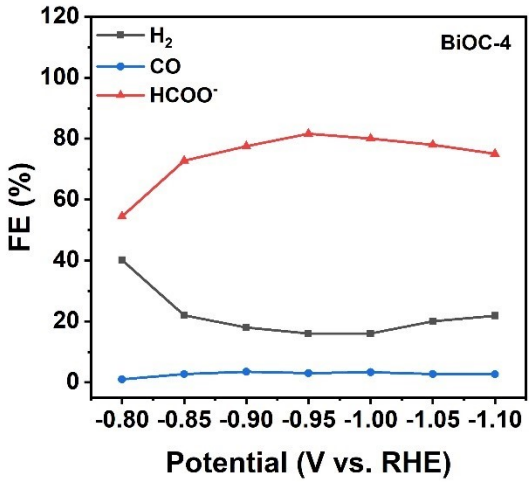

Figure S19. FEs of $HCOO^-$, CO and H_2 at various applied potentials on **BiOC–4**.

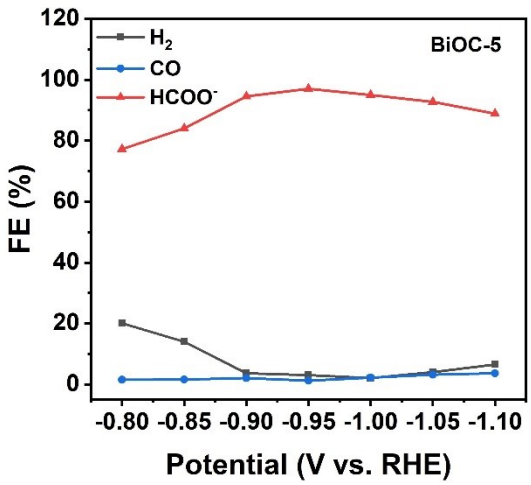

Figure S20. FEs of $HCOO^-$, CO and H_2 at various applied potentials on **BiOC–5**.

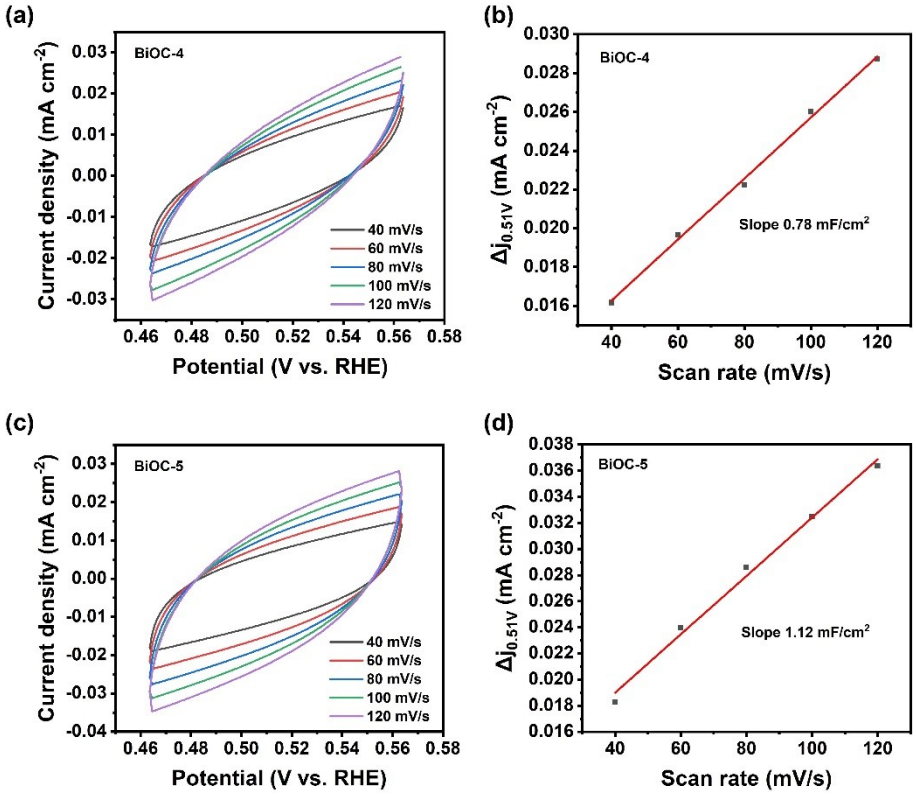

Figure S21. Cyclic voltammograms at the range of 0.46 to 0.56 V with different scan rates (40, 60, 80, 100, and 120 mV·s^{-1}) for **BiOC–4** (a) and **BiOC–5** (c). Linear fitting of double–layer capacitive currents ΔJ (Ja–Jc) at 0.51 V (vs.RHE) vs. scan rates to estimate ECSA for **BiOC–4** (b) and **BiOC–5** (d).

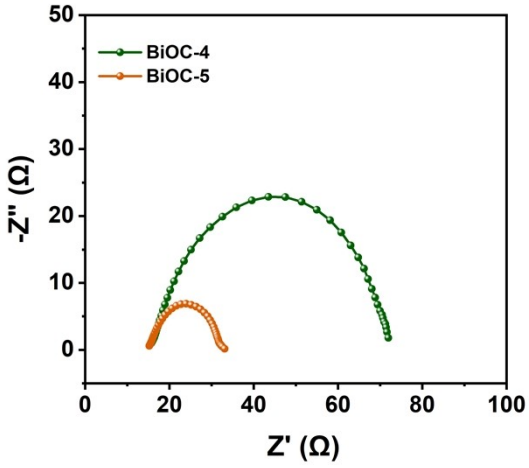

Figure S22. Nyquist plots for the **BiOC–4** and **BiOC–5**.

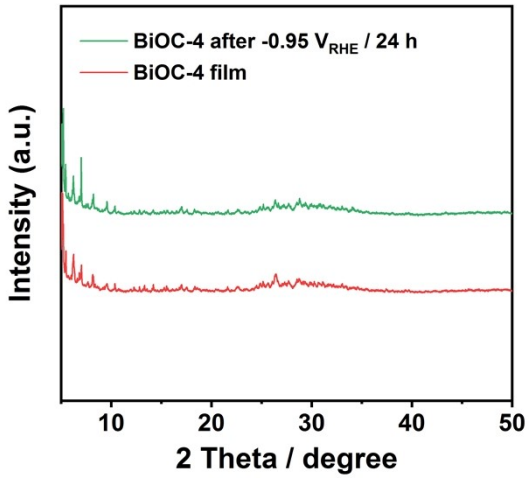

Figure S23. XRD patterns of **BiOC–4** before and after 24 h electrocatalysis.

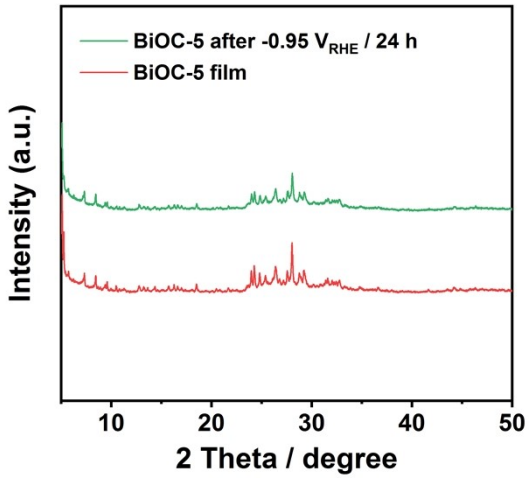

Figure S24. XRD patterns of **BiOC–5** before and after 24 h electrocatalysis.

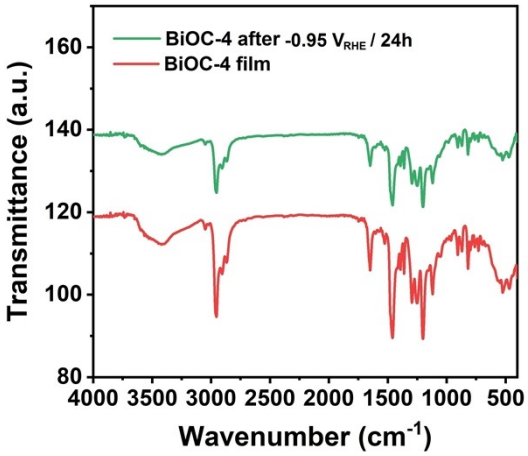

Figure S25. FT–IR spectra of **BiOC–4** before and after 24 h electrocatalysis.

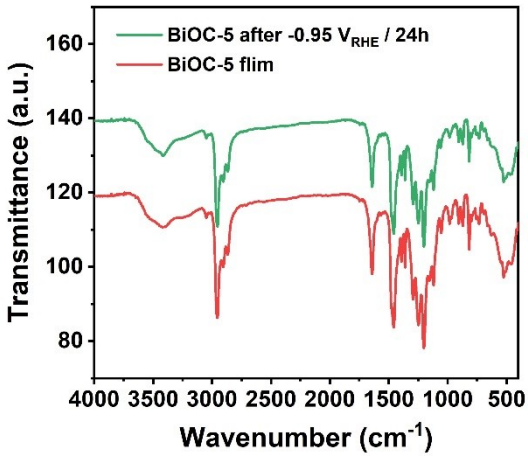

Figure S26. FT–IR spectra of **BiOC–5** before and after 24 h electrocatalysis.

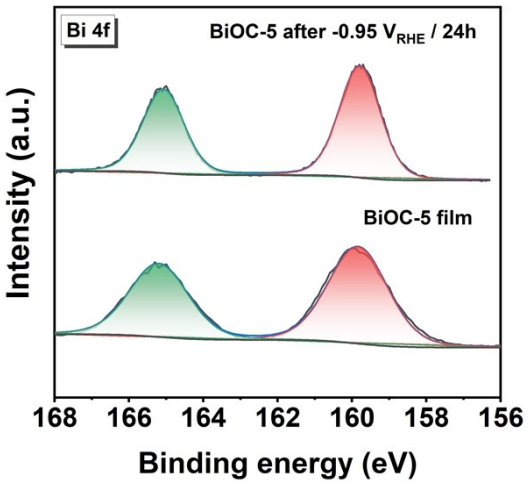

Figure S27. Bi 4f XPS spectra of **BiOC–5** before and after 24 h electrocatalysis.

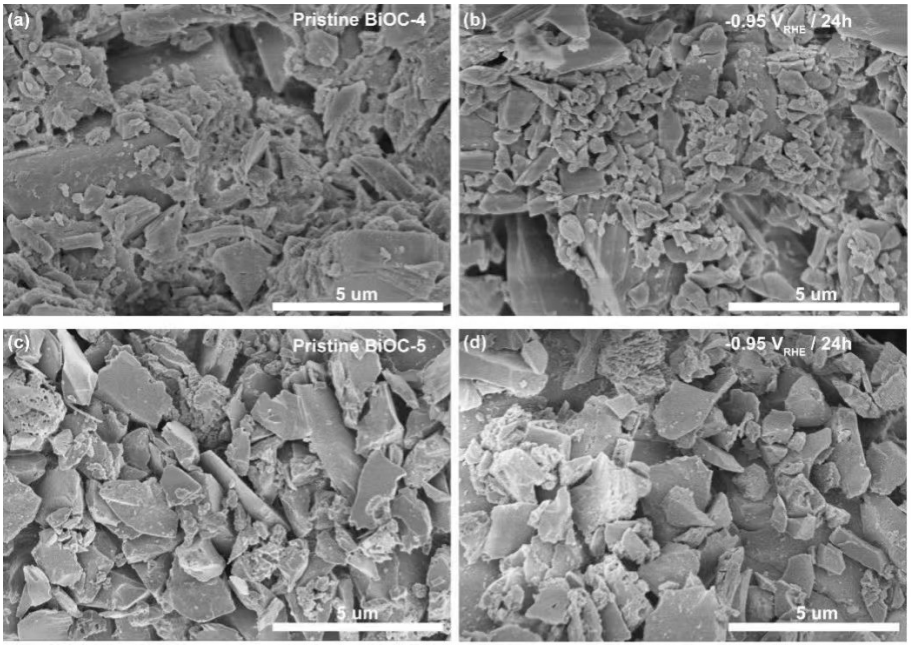

Figure S28. The SEM images of **BiOC–4** and **BiOC–5** before and after 24 h electrocatalysis.

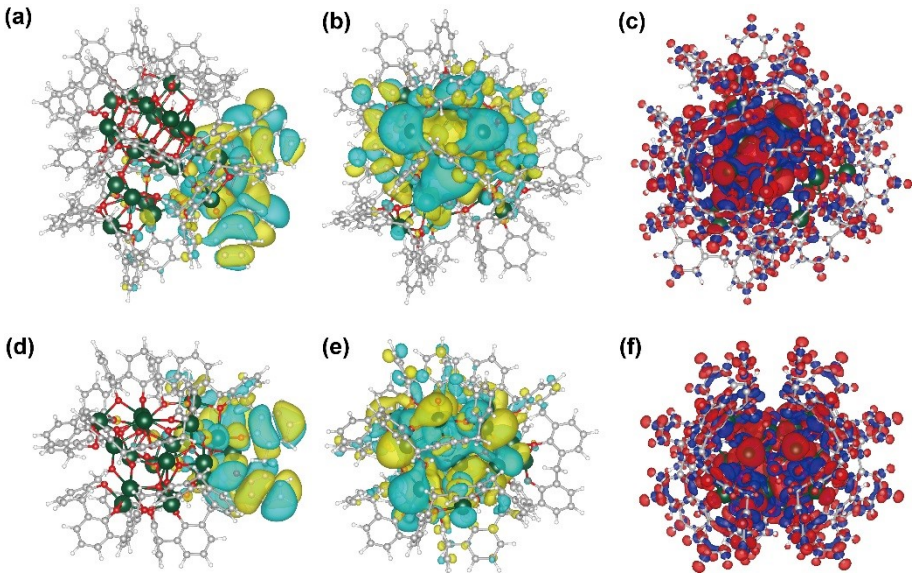

Figure S29. (a) and (d) the 3–D plot of HOMO of **BiOC–5** and **BiOC–4**, (b) and (e) the 3–D plot of LOMO of **BiOC–5** and **BiOC–4**, (c) and (f) the electron density difference of **BiOC–5** and **BiOC–4.**

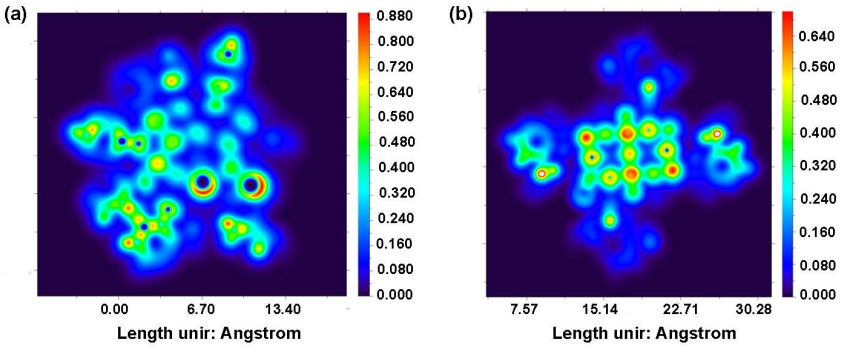

Figure S30. The localized orbital locator maps for **BiOC–4** (a) and **BiOC–5** (b).

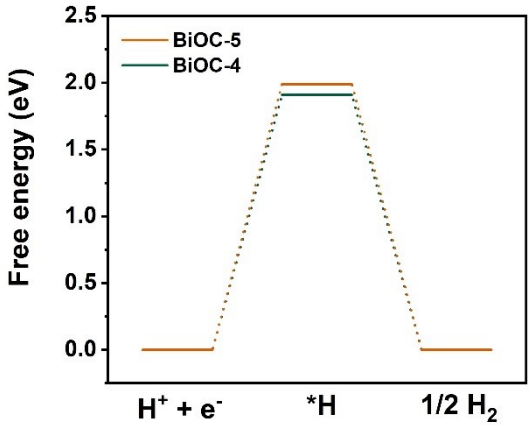

Figure S31. Free–energy diagrams for H_2 on **BiOC–4** and **BiOC–5**.

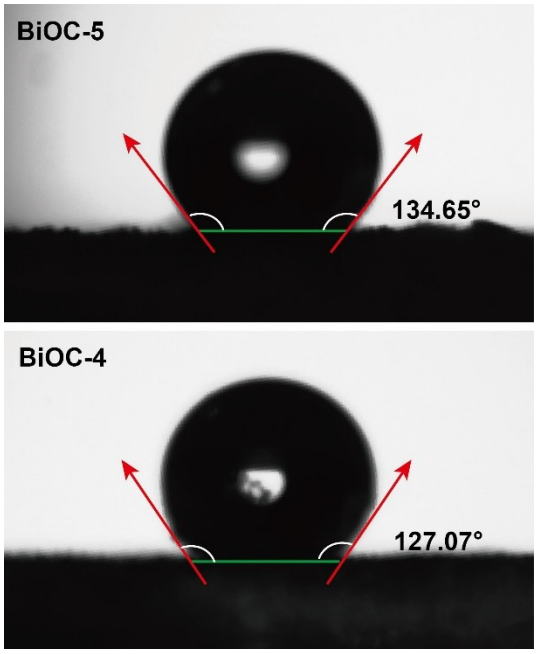

Figure S32. Contact angles of **BiOC–4** and **BiOC–5**.

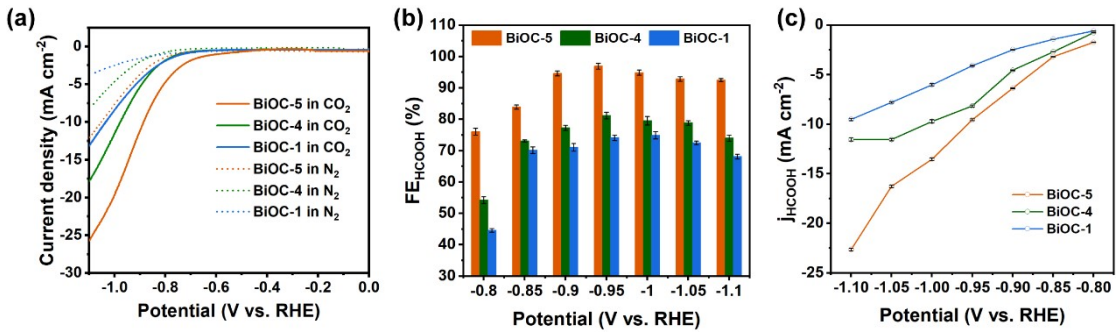

Figure. S33. (a) Polarization curves of **BiOC–1, BiOC–4** and **BiOC–5** in N_2 or CO_2 saturated 0.5 M $KHCO_3$. (b) Faradaic efficiencies of production and (c) the current densities of formate at different working potentials in CO_2-saturated 0.5 M $KHCO_3$ electrolyte for **BiOC–1, BiOC–4** and **BiOC–5**.

Table S1. The Crystallographic data for **BiOC–1** , **BiOC–2** , **BiOC–3, BiOC–4** , **BiOC–5** and **BiOC–6.**

Compound	**BiOC–1**	**BiOC–2**	**BiOC–3**	**BiOC–4**	**BiOC–5**	**BiOC–6**
Empirical formula	$C_{97}H_{140}Bi_4N_2O_{17}$	$C_{93}H_{121}Bi_4N_2O_{13}$	$C_{183}H_{231}NAlBi_8O_{27}$	$C_{294}H_{392}Bi_{20}N_9O_{61}$	$C_{384}H_{514}N_6Bi_{24}O_{79}$	$C_{694}H_{1067}Bi_{40}Mo_2N_{47}O_{172}$
Formula weight	2440.73	2312.83	4572.23	9202.73	11486.34	21357.71
Crystal system	Monoclinic	Triclinic	Tetragonal	Monoclinic	Tetragonal	Triclinic
Space group	$P2_1/c$	P–1	$I4_1/a$	$P2_1/c$	$I4_1/acd$	P–1
Temperature (K)	173.02	173.02	173.02	173.02	173.02	173.02
Wavelength (Å)	0.71073	1.54178	0.71073	1.54178	1.54178	1.54178
a (Å)	25.93(6)	16.570(4)	22.5610(4)	22.208(2)	35.3979(8)	22.5724(15)
b (Å)	13.52(3)	17.360(4)	22.5610(4)	37.888(4)	35.3979(8)	23.0297(14)
c (Å)	30.86(7)	19.896(5)	80.946(4)	44.949(4)	67.034(3)	36.361(2)
α (°)	90	67.924(11)	90	90	90	92.631(4)
β (°)	106.94(6)	78.114(12)	90	100.421(4)	90	103.905(4)
γ (°)	90	83.852(11)	90	90	90	115.578(3)
Volume (Å^3)	10351(41)	5187(2)	41201(5)	37197(6)	83994(5)	16306.2(18)
Z	4	2	8	4	8	1
$D_{calc.}$ /mg·m^{-3}	1.423	1.479	1.410	1.505	1.677	1.764
μ/mm^{-1}	6.827	13.492	6.864	18.543	19.745	21.269
F(000)	4312.0	2258.0	16936.0	15756.0	39936.0	8112.0
2Θ range for data collection (°)	4.71 to 50.528	4.872 to 128.1	4.768 to 50.164	4.046 to 128.272	5.646 to 127.73	4.988 to 128.292
Reflections	49915	72620	79501	297755	183395	179869

collected						
Independent reflections	18394 [$R_{(int)}$ = 0.0996]	17011 [$R_{(int)}$ = 0.0584]	18200 [$R_{(int)}$ = 0.1072]	61522 [$R_{(int)}$ = 0.0643]	17336 [$R_{(int)}$ = 0.0867]	52651 [$R_{(int)}$ = 0.1527]
Goodness–of–fit on F^2	1.014	1.076	1.022	1.021	1.042	1.023
Final R indices [I > 2sigma(I)]	R_1 = 0.0478, wR_2 = 0.1112	R_1 = 0.0581, wR_2 = 0.1356	R_1 = 0.0544, wR_2 = 0.1166	R_1 = 0.0638, wR_2 = 0.1712	R_1 = 0.0566, wR_2 = 0.1605	R_1 = 0.0895, wR_2 = 0.2027

Table S2 Summary and comparison of the catalytic performance with other Bi–based electrocatalysts materials for ECR to formic acid.

Catalyst	Electrolyte	Potential	FE_{HCOOH}	TOF
BiOC–5	**0.5 M $KHCO_3$**	**–0.95 V vs RHE**	**97%**	**405.7 h^{-1}**
Bi_3	0.5 M $KHCO_3$	–1.3 V vs RHE	96.37	377.55 h^{-1}
Bi-MOF	0.1 M $KHCO_3$	–0.9 V vs RHE	92.2	526.9 h^{-1}
Bi_2O_3NSs@MCCM	0.1 M $KHCO_3$	–1.265 V vs RHE	93.8%	/
MOF–derived Bi NPs	0.5 M $KHCO_3$	–0.97 V vs RHE	95%	16 × 10^3 h^{-1}
3.5 nm Bi NSs	0.1 M $KHCO_3$	–1.1 V vs RHE	92%	/
elongated Bismuth oxides	0.5 M $KHCO_3$	–0.9 V vs RHE	91%	/
Oxide–derived Bi	0.5 M $KHCO_3$	–0.82 V vs RHE	82%	/
Bi dendrite	0.5 M $KHCO_3$	–0.74 V vs RHE	89%	/
Bi_2O_3@C	0.5 M $KHCO_3$	–0.9 V vs RHE	92%	/
Bi_2O_3–NGQD	0.5 M $KHCO_3$	–0.9 V vs RHE	98.1%	/
POD–Bi	0.5 M $KHCO_3$	–1.16 V vs RHE	95%	/
Bi–ene	0.5 M $KHCO_3$	–0.88 V vs RHE	~100%	/
BiNS	0.5 M $NaHCO_3$	–1.06 V vs RHE	80%	/
Bi nanosheets	0.1 M $KHCO_3$	–1.1 V vs RHE	86%	/
SD–Bi	0.5 M $KHCO_3$	–0.75 V vs RHE	84%	/
BOCNS	0.5 M $NaHCO_3$	–0.7 V vs RHE	85%	/
BiO_x/C	0.5 M $NaHCO_3$	–1.13 V vs RHE	~93.4%	/

BiBrO templated	0.1 M $KHCO_3$	–0.9 V vs RHE	95%	/
Bi NSs	0.1 M $KHCO_3$	–0.98 V vs RHE	95.5%	/
Bi NTs	0.5 M $KHCO_3$	–1.1 V vs RHE	93%	/

Table S3 The vertical ionization energy of **BiOC–4** and **BiOC–5**

Oxidation state	**BiOC–4**	**BiOC–5**
0	0	0
+1	156.112	79.759

Reference

[1] G. Kresse, J. Hafner, *Phys. Rev. B* **1993**, *48*, 13115–13118.

[2] G.Kresse, J. Furthmüller, *Phys. Rev. B* **1996**, *54*, 11169–11186.

[3] G.Kresse, J. Furthmüller, *Comput. Mater. Sci.* **1996**, *6*, 15–50.

[4] J. P. Perdew, K. Burke, *Phys. Rev. Lett.* **1996**, 77, 3865–3868.

[5] P. E. Blöchl, *Phys. Rev. B* **1994**, *50*, 17953–17979.

[6] K. Mathew, V. S. C. Kolluru, S. Mula, S. N. Steinmann, R. G. Hennig, *J. Chem. Phys.* **2019**, *151*, 234101.

[7] K. Mathew, R. Sundararaman, K. Letchworth–Weaver, T. A. Arias, R. G. Hennig, *J. Chem. Phys.* **2014**, *140*, 084106.

[8] J. K. Nørskov, J. Rossmeisl, A. Logadottir, L. Lindqvist, J. R. Kitchin, T. Bligaard, H. Jónsson, *J. Phys. Chem. B* **2004**, *108*, 17886–17892.

[9] M. J. Frisch, G. W. Trucks, H. B. Schlegel, Gaussian 16, Revision C. 01, Gaussian, Inc., Wallingford CT, 2019.

[10] A. D. Becke, *J Chem Phys*. **1993**, *98*, 5648–5653.

[11] A. D. Becke, *J Chern Phys*. **1988**, *38*, 3098–3100.

[12] L. Tian, Multiwfn Manual, version 3.7(dev), Section 4.8.5.

[13] T. Lu, F. Chen, *J. Comput. Chem*. **2012**, *33*, 580–592.

[14] S. B. Liu, X. F. Lu, J. Xiao, X. Wang, X. W. Lou, *Angew. Chem. Int. Ed.* **2019**, *58*, 13828–13833.

[15] P. Lamagni, M. Miola, J. Catalano, M. S. Hvid, M. A. H. Mamakhel, M. Christensen, M. R. Madsen, H. S. Jeppesen, X. M. Hu, K. Daasbjerg, T. Skrydstrup, N. Lock, *Adv. Fund. Mater.* **2020**, *30*, 1910408.

[16] D. Z. Yao, C. Tang, A. Vasileff, Y. Zhi, Y. Jiao, S. Z. Qiao, *Angew. Chem. Int. Ed.* **2021**, *60*, 18178–18184.

[17] P. L. Deng, H. M. Wang, R. J. Qi, J. X. Zhu, S. H. Chen, F. Yang, L. Zhou, K. Qi, H. F. Liu, Y. X. Bao, *ACS Catal.* **2020**, *10*, 743–750.

[18] E. Bertin, S. Garbarino, C. Roy, S. Kazemi, D. Guay, *J. CO_2 Util.* **2017**, *19*, 276–283.

[19] J. H. Koh, D. H. Won, T. Eom, N. K. Kim, K. D. Jung, H. Kim, Y. J. Hwang, B. K. Min, *ACS Catal.* **2017**, *7*, 5071–5077.

[20] P. L. Deng, F. Yang, Z. T. Wang, S. H. Chen, Y. Z. Zhou, S. Zaman, Y. X. Bao, *Angew. Chem. Int. Ed.* **2020**, *132*, 10899–10905.

[21] Z. P. Chen, K. W. Mou, X. H. Wang, L. C. Liu, *Angew. Chem. Int. Ed.* **2018**, *130*, 12972–12976.

[22] S. S. He, F. L. Ni, Y. L. Ji, L. Wang, Y. Z. Wen, H. P. Bai, G. J. Liu, Y. Zhang,; Y. Y. Li, B. Zhang, H. S. Peng, *Angew. Chem. Int. Ed.* **2018**, *57*, 16114–16119.

[23] C. S. Cao, D. D. Ma, J. F. Gu, X. Y. Xie, G. Zeng, X. F. Li, S. G. Han, Q. L. Zhu, X. T. Wu, Q. Xu, *Angew. Chem. Int. Ed.* **2020**, *59*, 15014–15020.

[24] N. Han, Y. Wang, H. Yang, J. Deng, J. H. Wu, Y. F. Li, Y. G. Li, *Nat. Commun.* **2018**, *9*, 1320.

[25] W. J. Zhang, Y. Hu, L. B. Ma, G. Y. Zhu, P. Y. Zhao, X. l. Xue, R. P. Chen, S. Y. Yang, J. Ma, J. Liu, Z. Jin, *Nano Energy* **2018**, *53*, 808–816.

[26] Y. Zhang, F. W. Li, X. L. Zhang, T. Williams, C. D. Easton, A. M. Bond, J. Zhang, *J. Mater. Chem. A.* **2018**, *6*, 4714–4720.

[27] Y. Zhang, X. L. Zhang, Y. Z. Ling, F. W. Li, A. M. Bond, J. Zhang, *Angew. Chem. Int. Ed.* **2018**, *57*, 13283–13287.

[28] C. W. Lee, J. S. Hong, K. D. Yang, K. Jin, J. H. Lee, H. Y. Ahn, H. Seo, N. E. Sung, K. T. *ACS Catal.* **2018**, *8*, 931–937.

[29] F. P. G. D. Arquer, O. S. Bushuyev, P. De Luna, C. T. Dinh, A. Seifitokaldani, M. I. Saidaminov, C. S. Tan, L. N. Quan, A. Proppe, M. G. Kibria, S. O. Kelley, D. Sinton, E. H. Sargent, *Adv. Mater.* **2018**, *30*, 1802858.

[30] J. Yang, X. L. Wang, Y. T. Qu, X. Wang, H. Huo, Q. K. Fan, J. Wang, L. M. Yang, Y. E. Wu, *Adv. Energy Mater.* **2020**, *10*, 2001709.

[31] K. Fan, Y. F. Jia, Y. F. Ji, P. Y. Kuang, B. C. Zhu, X. Y. Liu, J. G. Yu, *ACS Catal.* **2020**, *10*, 358–364.

[32] T. P. Thanh, D. Rahman, F. Zelio, Z. P. Ma, R. Amal, A.Tricol, *Adv. Fund. Mater.* **2020**, *30*, 1906478.

[33] Y. T. Wang, Y. H. Li, J. Z. Liu, C. X. Dong, C. Q. Xiao, L. Cheng, H. L. Jiang, H. Jiang, C. Z. Li, *Angew. Chem. Int. Ed.* **2021**, *60*, 7681–7685.